A magnetotelluric investiagation of shallow conductivity sources beneath the Cascadia Volcanic Arc

by
L Roy Bonner IV

A PROJECT

submitted to

Oregon State University

University Honors College

in partial fulfillment of
the requirements for the
degree of

Honors Baccalaureate of Science in Physics
(Honors Scholar)

Presented May 26th, 2015
Commencement June 2015

AN ABSTRACT OF THE THESIS OF

L Roy Bonner IV for the degree of Honors Baccalaureate of Science in Physics presented on May 26th , 2015. Title: A magnetotelluric investigation of shallow conductivity sources beneath the Cascadia Volcanic Arc.

Abstract approved: _____

Adam Schultz

The Cascade Volcanic Arc has been the subject of extensive study in the past due to its active volcanism and its proximity to metropolitan areas. The triangle formed by the volcanoes Mount Saint Helens, Mount Rainier, and Mount Adams is of particular interest because of this potential danger and the geological complexity of the area. Anomalously high conductivity, known as the Southern Washington Cascades Conductor (SWCC), was detected in portions of the region and attributed to trapped marine sediment and partial melt from volcanism in different studies. The magnetotelluric method was used to study the shape and potential causes of the SWCC through acquiring surface electric and magnetic field data throughout the region in 2014, as part of the NSF funded iMUSH project. A linear northeast-to-southwest profile of stations was analyzed to produce a two-dimensional conductivity cross-section through inversion. The best fitting conductivity model was checked with the preexisting studies and found to confirm the existence of the SWCC in certain areas. The model also showed signs of marine sediment and volcanism presence in different portions of the region, though geological complexity and data set limitations prevented a definitive conclusion from being drawn.

Key Words: magnetotellurics, MT, SWCC, conductivity, Cascades

Corresponding e-mail address: bonnerl@onid.orst.edu

A magnetotelluric investigation of shallow conductivity sources beneath the Cascadia Volcanic Arc

by
L Roy Bonner IV

A PROJECT

submitted to

Oregon State University

University Honors College

in partial fulfillment of
the requirements for the
degree of

Honors Baccalaureate of Science in Physics
(Honors Scholar)

Presented May 26th , 2015
Commencement June 2015

Honors Baccalaureate of Science in Physics project of L Roy Bonner IV presented on May 26th , 2015.

APPROVED:

Adam Schultz, Mentor, representing College of Earth, Ocean, and Atmospheric Sciences

Albert Stetz, Committee Member, representing Physics

David Roundy, Committee Member, representing Physics

Toni Doolen, Dean, University Honors College

I understand that my project will become part of the permanent collection of Oregon State University, University Honors College. My signature below authorizes release of my project to any reader upon request.

L Roy Bonner IV, Author

Table of Contents

List of Figures

Section 1 – Introduction

1.1 Motivation and Objective

The dominant electromagnetic geophysical factor in the Cascadia triangle is described by an anomalously high and shallow conductivity, which is known as the Southern Washington Cascades Conductor (SWCC). High conductivity relates to the strong ability of electric current to flow through a material, so trapped marine sediment and partial melt from volcanism can explain the anomaly, as suggested by the work of Stanley *et al.*(1990) and Hill *et al.* (2009) respectively. Both explanations for the conductivity have large implications on the geological formation and properties of the area. Assessing the presence of partial melt and magma generation helps determine if the volcanoes have tertiary magmatic structures or interconnected magma chambers, which is important for evaluating potential lava production and improving eruption detection techniques. Confirming the geological properties of the area is also economically important because oil can develop within the pores of deposited sediment and geothermal plants can be built on areas of magma generation (Stanley, 1990). The areas that were studied to reach both conclusions do not overlap or cover the entire region, so additional research is needed. The imaging technique known as magnetotellurics (MT) generates a resistivity landscape that is dependent on ground composition, which makes it useful for determining the cause of the anomaly. The goal of this experiment was to conduct a 2-dimensional MT survey that bridged the areas for both results to enable comparison and gain a better understanding of the volcanic triangle.

1.2 Geological Setting and Principles

1.2.1 Geological Background and Conductivity Properties

The main geological principle concerning the Cascades involves volcanism produced from subduction between the oceanic Juan de Fuca/Gorda Plate and the overriding continental North American Plate. Subduction primarily generates magma through mantle decompression and slab dehydration. Decompression occurs when the rigid descending plate introduces an upward normal force on the overriding plate, which counteracts the downward lithostatic pressure due to the weight of the material above the plate boundary (Tarbuck, 2013). Pressure is directly related to melting point, so the release of pressure lowers the boundary material's melting point below the temperature of the region, which leads to melting. The other method of melt generation comes from the introduction of water into the mantle as descending oceanic plates dehydrate. Mantle rock is generally comprised of silicates that have lower melting points when hydrated, so the introduction of water assists in the initial melting near the subduction boundary (McGary, 2014). The presence of water can also decrease rock uniformity and cause uneven heating to produce more melting (Kelbert, 2009). The introduction of partial melt from both sources causes the rock to be more buoyant and thus rise above the surrounding rock. Temperature and pressure increase with depth, so the rock maintains its high temperature while reducing its pressure as it rises, which leads to further melting

and upwelling. This cycle of increased melting and rising from lowered pressure causes the material to transition from rock to magma in its journey from the mantle to the crust. Magma becomes trapped in the crust or extruded as lava depending on the pathway that the material takes. A diagram for the general form of a subduction zone and where melting and magma upwelling occurs is shown below in Fig. 1.1.

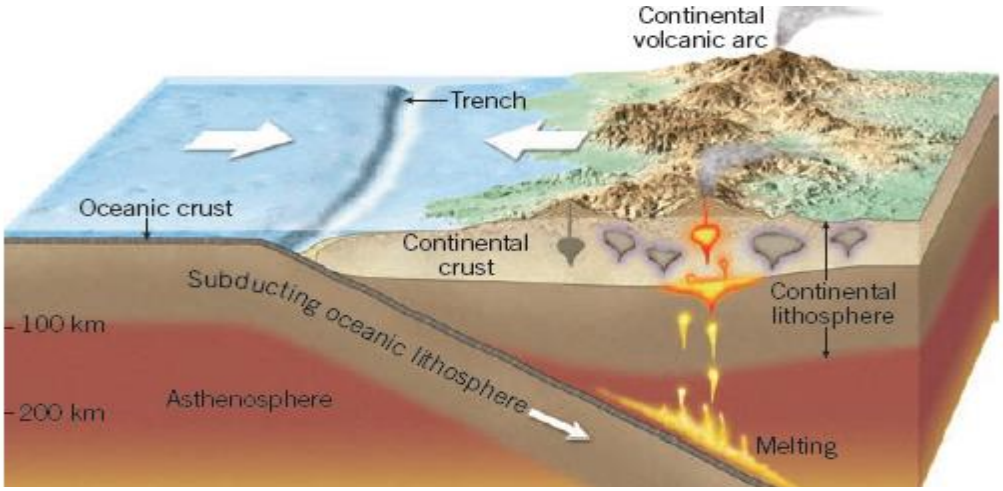

Fig. 1.1: Model of structure vs. location and depth for general subduction zone (Tarbuck, 2013, pg. 56).

The location of ocean water and melt in relation to magma generation and upwelling can be detected due to the relatively high conductivity of the two geothermal liquids (McGary 2014). Ocean water is highly conductive because it contains sodium and chlorine ions that serve as electrolytes. Melt removes the crystalline structure of silicates by turning them into liquids, which allows for easier ion flow through the material and thus greater conductivity than the surrounding rock (Ni, 2011). The percentage of melt within the rock increases as it approaches the surface from decompressional melting resulting from upwelling, so a rising increase in conductivity on a resistivity block section of the area might indicate the presence of a magma chamber or an area of hydrothermal fluid accumulation. An example of this conductivity shape is shown below in Fig. 1.2, though it also depicts the plate subduction and the point of initial melt from water content and decompression The ability to identify the presence of melt is useful for differentiation from other high conductivity sources, such as marine sediment with high water content, and for determining the implications of the experimental results.

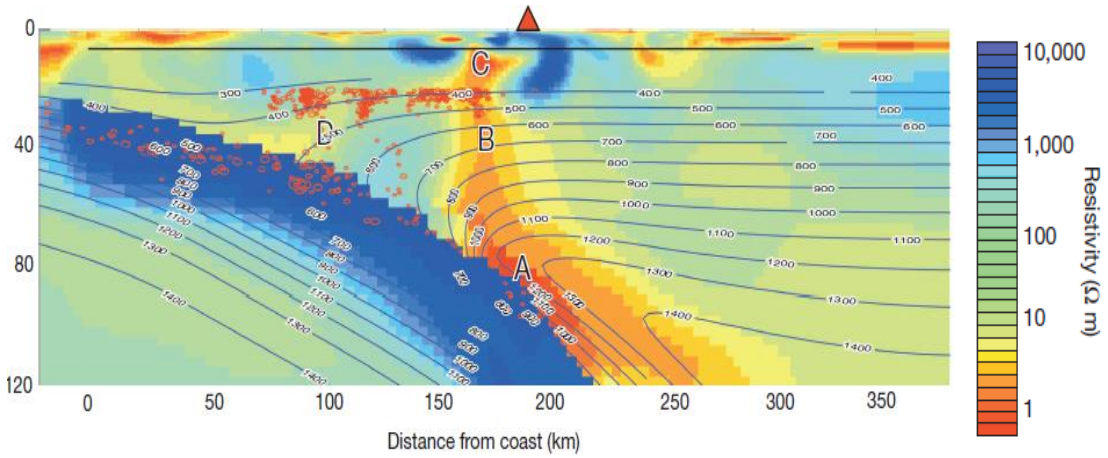

Fig. 1.2: Resistivity vs. depth and location of Mount Rainier resistivity block section, with earthquake locations shown as red dots. The initial melt location occurs around point A, mantle upwelling occurs along the column of points B and C, and Mount Rainier is located at the triangle (McGary, 2014, pg. 339). Image reproduced with permission from Nature Publishing Group.

1.2.2 Southern Washington Cascades Conductor

The specific geology of the triangle formed by Mount Saint Helens, Mount Rainier, and Mount Adams is predominantly characterized by a large portion of Quaternary Period (2.6 Mya – Present) volcanic rocks relating to recent lava flows, and Eocene Epoch (56 – 34 Mya) marine and non-marine sedimentary rocks that have multiple possible origins (Stanley, 1992). There is also an anomalous conductive grouping of rocks that is up to 15 kilometers thick and begins at a range of 1 to 10 km depth throughout several portions of the area that is called the Southern Washington Cascades Conductor (SWCC) (Stanley, 1984). There is currently a debate concerning whether the conductive anomaly can be attributed to trapped marine sediment or partial melt. Marine sediment is highly conductive because of its high ocean water and clay mineral content. Clay minerals can be conductive due to concentration of charge on their surface that gives them a high ion exchange capacity (Revil, 1998). The high conductivity of ocean water and partial melt was previously mentioned, along with the conductive form of melt and magmatic chambers, so the shape of the conductivity can be used to determine the nature of the SWCC.

The anomaly was originally studied through 2D magnetotelluric cross-sections, seismic reflection studies, and well logging. Magnetotellurics gave the general shape of the anomaly in the areas studied and determined that the resistivity of the SWCC was 2 to 5 Ωm in most locations, which corresponds to typical marine sediment (Stanley, 1984). Seismic reflection was analyzed along the anticlines of the area, and an east-dipping layer was found that corresponded to a portion of the SWCC (Stanley, 1992). The anticlines brought trapped Tertiary Period (66 – 2.6 Mya) marine sediment to near surface from stress that caused the rock layers to bend, which suggested that trapped marine sediment could explain the conductance. Logging of wells in the area further supported the marine sediment cause, due to the presence of Eocene marine sandstone and shale at the expected depths with resistivities matching those measured in the MT survey (Stanley

1984). The agreement between the multiple geophysical surveys led to the conclusion that trapped marine sediment was the most probable cause for the majority of the SWCC. A diagram of the lithology, MT cross-sections, anticlines, and wells is shown below in Fig. 1.3.

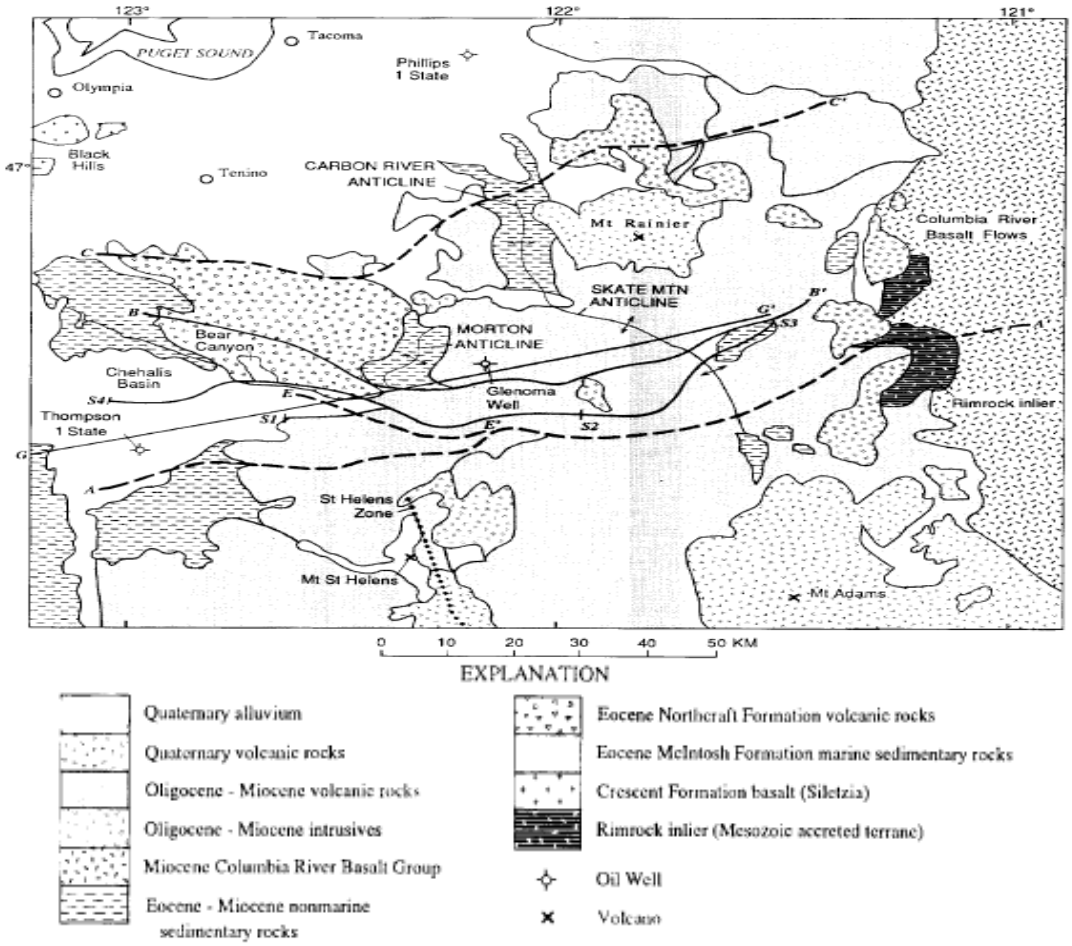

Fig. 1.3: Diagram of southern Washington Cascades lithology, anticlines, volcanoes, wells, and the 2D MT cross-sections used for the detection of the SWCC (Stanley, 1992).

The presence of trapped marine sediment, and likely all Eocene marine sediment in the area, can be explained by two different tectonic actions. Compression and trapping of accreted Eocene marine sediment during the subduction driven collision that formed the Oregon and Washington coastal range is one of the possible explanations (Stanley, 1987). Tectonic stress from a collision is relieved by the creation of mountain ranges and basins, so it is possible that the sediment was deposited and then buried in the newly formed basin caused by the mountain building event. The other explanation involves the creation of a pull-apart basin from plate extension that opened up a rift for the sediment to be deposited in and then trapped (Stanley, 1992). Tension produced from rifting or stretching within a continental plate also produces mountains and basins that can explain the trapping, yet no known pull-apart basins exist in Oregon or Washington (Stanley, 1992). Basins that were created from subduction collisions are prevalent throughout the west coast of the United States and Canada, so it is far more likely that the trapped

sediment can be explained through this tectonic process (Stanley, 1992). This gives an insight into the geological processes that occurred in that region and time if the conductance is caused by trapped marine sediment.

The other main explanation for the SWCC involves the presence of melt caused by the volcanism of the area. This conclusion was reached from the agreement between the 2D and 3D portions of a recent magnetotelluric survey in the area, with the 2D results displayed below in Fig. 1.4 (Hill, 2009). The cross-section shows a connection between Mount Saint Helens, Mount Adams, and a mid-crustal conducting slab that corresponds to the SWCC. Rising conductivity from the slab into the volcanoes suggests that the slab contains partial melt. A melt of 2-12% would explain the conductivity, as would it upwell into the magma chambers of the volcanoes to explain the form of the cross-section (Hill, 2009). Mount Saint Helens and Mount Adams extrude a mixture of basalt and silicic magmas, with the basalt originating from partial melting of the mantle wedge (Defant, 1993). Melting of the subducting slab would normally produce silicic magma, though the results of the survey imply that the magma source is instead from partial melt in this mid-crustal conducting slab, which would help to identify the magmatic structure of the volcanoes (Hill, 2009).

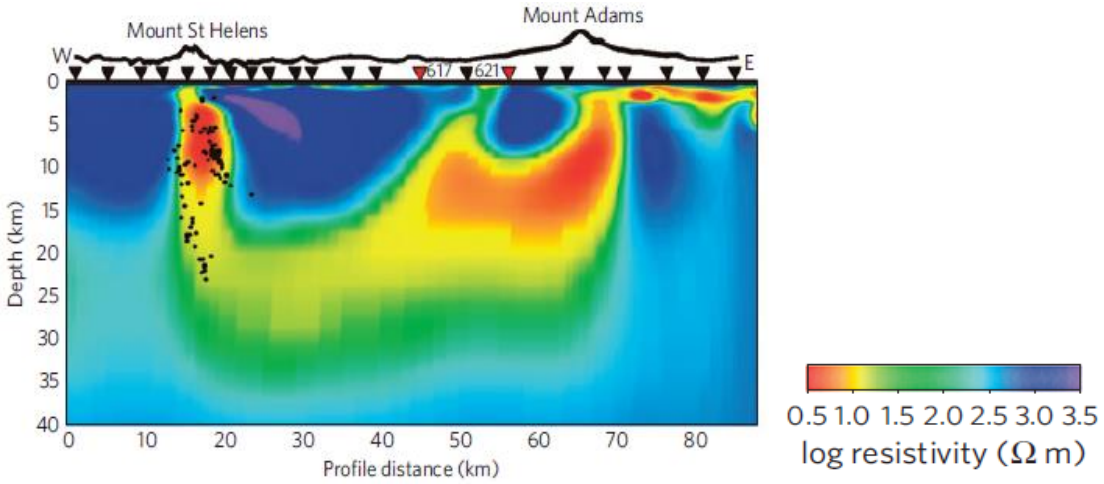

Fig. 1.4: Block section of resistivity vs. depth along cross-section running east from Mount Saint Helens to Mount Adams (Hill, 2009). Image reproduced with permission from Nature Publishing Group.

Trapped marine sediment and partial melt within a mid-crustal conducting slab are both well-supported and convincing arguments for the nature of the SWCC, though they are also incomplete explanations of the entire anomaly. The primary issue with the marine sediment conclusion is the maximum depth of the high conductance region. Marine sediment is highly conductive because of its high ocean water and clay mineral content, though it loses water and the conductive property of the clay minerals when it undergoes metamorphosis from the pressure and temperature introduced from burial (Hill, 2009). Metamorphosis should occur by a depth of 15 kilometers, yet the conductivity remains high past that depth in certain places (Hill, 2009). The presence of graphite in the sediment would allow for it to become a metamorphic rock with the proper conductivity, yet graphitic metamorphic rocks are rare in the area (Stanley, 1992). Geothermal fluid present in the metamorphic rocks from partial melt due to volcanism

would also produce the correct conductivity, though the cross-section depicting the mid-crustal slab did not show any east-dipping conductance related to the marine SWCC (Hill, 2009).

Lack of agreement between the models does not invalidate the marine results, because the MT cross-sections were taken in different parts of the area. Three MT cross-sections, two anticline seismic studies, and three wells spread out across the area were used to justify the marine conclusion, while one MT cross-section and a 3D array along the bottom of the triangle were analyzed for the mid-conducting slab conclusion. This lack of location overlap makes it difficult to resolve the two explanations and to extend either cause to the whole region. Marine sediment does not properly address deep conductivity and partial melt does not answer the presence of trapped marine sediment or conductivity in other portions of the volcano triangle. It is possible that one or both of the explanations are correct, though more information is needed that bridges the surveys to choose sides, which is the goal of this experiment.

1.3 The Magnetotelluric Method

1.3.1 Impedance and Resistivity Derivations

The governing principles of magnetotellurics can be derived from Maxwell's equations as applied to a conductive material. These equations relate the divergence and curl of the electric field *E* and the magnetic field *B* to electric permittivity ε, magnetic susceptibility μ, free volume charge ρ_f, and conductivity σ. Maxwell's equations are given by

$$\boldsymbol{\nabla} \cdot \boldsymbol{E} = \frac{\rho_f}{\varepsilon}, \tag{1a}$$

$$\boldsymbol{\nabla} \times \boldsymbol{E} = \frac{-\partial \boldsymbol{B}}{\partial t}, \tag{1b}$$

$$\boldsymbol{\nabla} \cdot \boldsymbol{B} = 0, \tag{1c}$$

and

$$\boldsymbol{\nabla} \times \boldsymbol{B} = \mu\sigma\boldsymbol{E} + \mu\varepsilon\frac{\partial \boldsymbol{E}}{\partial t} \quad \text{(Griffiths, 2014).} \tag{1d}$$

Magnetotelluric signals are generated from the inductive effects of solar wind and lightning. The solar wind is essentially a plasma stream of particles from the sun. Protons and electrons from the solar wind separate in the earth's magnetosphere and ionosphere to create an electric field that fluctuates based on the density and velocity of the plasma (Simpson, 2005). This electric field creates a varying ionospheric current that induces a magnetic field that diffuses into the Earth, with a corresponding electric field at the Earth's surface given by Faraday's Law of Induction (Eq. 1b) (Simpson, 2005). The externally induced magnetic field dominates the geomagnetic spectrum at frequencies between approximately 10^{-5} Hz and 1 Hz. A diagram of plasma charge differentiation and the resulting magnetosphere is shown below in Fig. 1.5. Lightning also induces

magnetic fields in the earth's surface, through discharging electromagnetic signals known as spherics that propagate within a waveguide between the surface and ionosphere (Garcia, 2002). These spherics have a broad range of frequencies above 1 Hz and they also establish resonances within the ionsphere that dictate specific properties of the induced magnetic fields (Garcia, 2002). Magnetotelluric signals have frequencies well below 10^5 Hz, so they are predominantly diffusive and the displacement current $\mu\varepsilon\, \partial \boldsymbol{E}/\partial t$ in Eq. 1d can be neglected. This simplification is important because it implies that MT signals are described by diffusion relating to a chain of inducing electromagnetic fields rather than a wave equation that describes a multi-layered optical system. Effectively, the primary induced magnetic field generates a secondary electric field that has its own secondary magnetic field that in turn diffuses and so on, rather than continuous source waves that reflect and transmit through conductive interfaces.

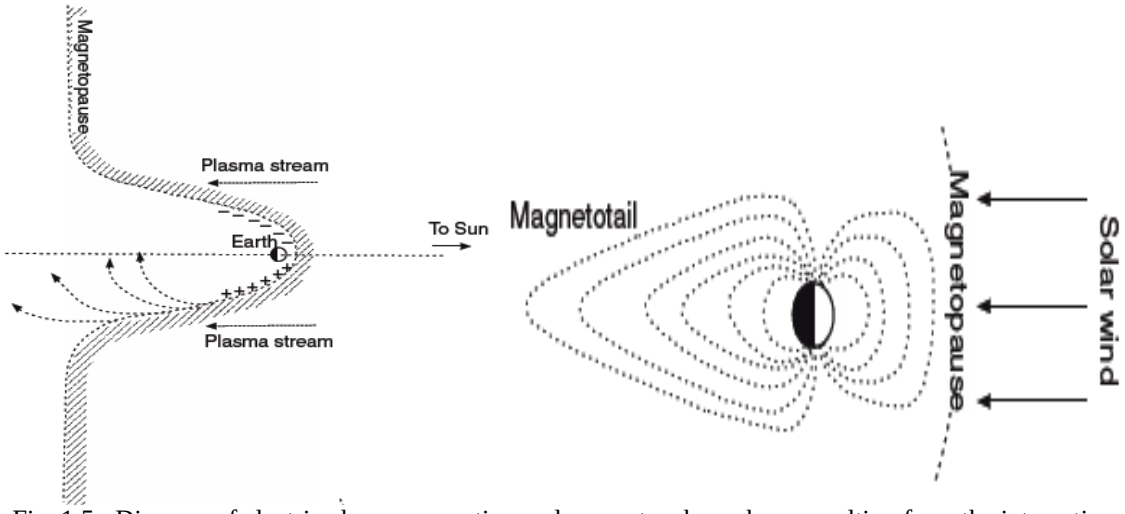

Fig. 1.5: Diagram of electric charge separation and magnetosphere shape resulting from the interaction between the solar wind and magnetosphere, shown on left and right respectively (Simpson, 2005, pg. 4).

The derivations that constitute the rest of Section 1.3 follow Chapter 2 in Simpson (2005) and Chapter 6 of Telford (1990). Magnetotelluric signals are produced far enough away from the surface to be considered planar and thus simply expressed as a complex exponential function with a wave number *k*, propagation direction *r*, angular frequency *w*, and time *t*. The general form for an x-direction polarized wave with zero phase Φ is

$$\boldsymbol{E} = E_0 e^{-i(k\cdot r - wt)} = \boldsymbol{E_x} e^{-i(kz - wt)} \tag{2a}$$

and

$$\boldsymbol{B} = B_0 e^{-i(k\cdot r - wt)} = \boldsymbol{B_y} e^{-i(kz - wt)} \ . \tag{2b}$$

The magnetic field *H* for a 1-dimensional conductivity system can be derived in terms of the electric field *E* through Eq. 1b and

$$\boldsymbol{\nabla \times E} = \frac{-\partial \boldsymbol{B}}{\partial t} \rightarrow \boldsymbol{B_y} = \mu \boldsymbol{H_y} = -\int \frac{\partial \boldsymbol{E_x}}{\partial z} dt = \frac{1}{iw}\frac{\partial \boldsymbol{E_x}}{\partial z} = \frac{-k\boldsymbol{E_x}}{iw}. \tag{3}$$

The *E* and *H* fields can be used to determine the magnitude of the impedance *Z*, which is effectively a complex resistance of the material that the signal diffuses through, via

$$|Z| = \left|\frac{E}{H}\right| \tag{4}$$

$$\left|Z_{xy}\right| = \left|\frac{E_x}{H_y}\right| = -\frac{iw\mu}{k} = -\left|Z_{yx}\right|$$

$$\boldsymbol{Z} = \begin{bmatrix} Z_{xx} & Z_{xy} \\ Z_{yx} & Z_{yy} \end{bmatrix}$$

$$= |Z|e^{\Phi} = |Z|e^{\tan^{-1}\left(\left|\frac{E}{H}\right|\right)}.$$

For the case where the electrical conductivity of the Earth is taken to vary in two dimensions (vertically, and along one horizontal direction), the *x*-direction corresponds to the field orientation parallel to a *z*-direction vertical interface between two materials of different conductivities, while the *y*-direction involves the orthogonal horizontal orientation. The 2-dimensional conductivity case can be generalized from these computations by splitting the *E* and *H* fields into *x* and *y* components that form the transverse electric (E_x and H_y) and transverse magnetic (E_y and H_x) modes relating to opposite orientations between each field and the interface. This splitting results in different values of Z_{xy} and Z_{yx} that lead to different resistivities of ρ_e and ρ_m respectively. Resistivity corresponds to a materials innate opposition to electron flow, which is independent of its shape or size unlike resistance. For the case of two-dimensional conductivity structure, when measured in the coordinate frame parallel to geoelectric strike direction, the diagonal elements of the impedance tensor Z_{xx} and Z_{yy} are zero. Geoelectric strike direction corresponds to the direction orthogonal to a conductive layer, similar to geologic strike being perpendicular to the dip direction of a rock layer. The impedance tensor elements are non-zero only in the case of three-dimensional conductivity variations, or if the impedance is measured in a coordinate frame that is rotated relative to the geoelectric strike direction. In such a case, the impedance tensor can be rotated within a coordinate frame that minimizes the diagonal terms. A special case exists when 2-D conductivity structure is overlain by a thin 3-D layer, which has a significant impact on the magnitude of the impedance tensor elements, but not on their phase. The phase, Φ, is given in Eq. 4 from the general form of a complex function.

The resistivity, ρ, equal to the inverse of conductivity σ, can be derived through

$$\boldsymbol{\nabla} \times (\boldsymbol{\nabla} \times \boldsymbol{E}) = \boldsymbol{\nabla}(\boldsymbol{\nabla} \cdot \boldsymbol{E}) - \boldsymbol{\nabla^2 E} \tag{5a}$$

$$= 0 - \boldsymbol{\nabla^2 E} = \frac{-d}{dt}(\boldsymbol{\nabla} \times \boldsymbol{B}) = \frac{-d}{dt}(\mu\sigma \boldsymbol{E})$$

thus

$$\boldsymbol{\nabla^2 E} = -\mu\sigma\frac{d\boldsymbol{E}}{dt}.$$

$$\boldsymbol{\nabla^2 E} = \boldsymbol{k^2 E} = -\mu\sigma\frac{d\boldsymbol{E}}{dt} = -iw\mu\sigma\boldsymbol{E}\,, \tag{5b}$$

so

$$\boldsymbol{k} = \sqrt{-iw\mu\sigma}$$

and

$$\rho_e = \frac{\left|\frac{E_X}{H_y}\right|^2}{w\mu}$$

$$\rho_m = \frac{\left|\frac{E_y}{H_x}\right|^2}{w\mu}\,.$$

These simplifications include setting the gradient of the divergence of *E* and the displacement current $\mu\varepsilon dE/dt$ to 0. The gradient of the divergence of *E* is zero because all current, and thus electric field change, flows along the interface where *E* is polarized. Displacement current was previously mentioned to be negligible due to the low frequency of the signal. The wave vector *k* can be used to solve for ρ in terms of *E* and *H* from Eq. 4, which allows for a resistivity cross section to be constructed from surface electromagnetic measurements.

1.3.2 Skin Depth Effect and Signal Uniqueness

The skin depth effect δ, which shows the inverse relationship between frequency and depth of penetration, is determined by solving for the point where the magnitude of the primary magnetic field is attenuated to 1/ε of its original value by conversion of its energy into electric current, which is dissipated through ohmic heat loss within the conducting medium. The magnitude of *B* from Eq. 2b can be represented with the form of k from Eq. 5b, which can be split into a real and imaginary part. The magnitude of *B* is time independent and thus has the form

$$|\boldsymbol{B}(\boldsymbol{z})| = \left|\boldsymbol{B_x} e^{\pm(1-i)\sqrt{\frac{w\mu\sigma}{2}}z}\right| = \boldsymbol{B_x} e^{\sqrt{\frac{w\mu\sigma}{2}}z}\quad, \tag{6}$$

and

$$\frac{|\boldsymbol{B}(\boldsymbol{\delta})|}{|\boldsymbol{B_x}|} = \frac{1}{e}$$

when

$$\delta = \sqrt{\frac{2}{w\mu\sigma}} = \sqrt{\frac{1}{\pi f\mu\sigma}} \approx \sqrt{\rho}\,\frac{503}{f}\,,$$

which gives the form of the skin depth effect. The exponentially increasing term in the magnitude of *B(z)* is removed to prevent the magnetic field from increasing to infinity as the depth *z* increases. This relationship between frequency and depth is useful for determining the measuring times required to study specific depths to survey the desired region.

The resistivities calculated in Eq. 5b are called apparent resistivities, because they are averages based on the field values of the entire conductivity layer relating to the impedance tensor. The Earth does not have homogeneous 2-dimensional layers, nor can its exact resistivity variations be directly determined, so the forward problem of obtaining resistivity from measured surface field values does not work. Resistivity can be calculated by the inverse problem, where the variations are estimated from the ratios of the electric and magnetic fields measured vs. frequency and locations, though there are multiple possible solutions, which introduces non-uniqueness (Parker, 1983). Adding conditions to the problem, such as maximizing model smoothness, allows for models relating to specific solutions to be essentially unique.

1.4 Inversion

1.4.1 The Principles of Inversion

Inversion is the process of solving linear or non-linear systems by proposing models of simulated data and then using direct or indirect solution methods to generate results that can be compared to the observed data (Parker, 1977). In the case of magnetotellurics, the starting reference model is usually a homogeneous half-space that contains the same resistivity in each block of the model. Other starting models can be used if there is previous knowledge about the area, though starting with a homogeneous model helps to keep the results unbiased from not specifying the resistivity form. The resistivity of each of the blocks in the model is used to numerically solve the forward Maxwell equations for the 2-dimensional transverse electric and magnetic modes given by

$$\frac{\partial^2 \boldsymbol{E_x}}{\partial y^2} + \frac{\partial^2 \boldsymbol{E_x}}{\partial z^2} + i\omega\mu\sigma_e \boldsymbol{E_x} = 0 \tag{7}$$

and

$$\frac{\partial}{\partial y}\left(\rho_m \frac{\partial \boldsymbol{H_x}}{\partial y}\right) + \frac{\partial}{\partial z}\left(\rho_m \frac{\partial \boldsymbol{H_x}}{\partial z}\right) + i\omega\mu \boldsymbol{H_y} = 0 \tag{8}$$

respectively, with the equations for apparent resistivity found in Eq. 5b (Rodi, 2001).

Numerically solving Maxwell's equations is computationally intensive, and the inversion process typically requires iteratively generating candidate models that each have forward solutions and misfits between the observed data (impedance or apparent resistivity and phase) and model. An inversion method is chosen to successfully and iteratively reduce the misfit based on which model parameters are varied, so that the process converges to a model that fits the data. The most common approach within magnetotellurics is to construct a partial derivative Jacobian matrix, where each element contains a value proportionate to the change in misfit with respect to the change in a model parameter, with the misfit determined through an objective function (Rodi, 2001). The objective function relates the data, error, and model vectors for each block through the Jacobian and several other matrices representing parameters that narrow potential solutions. The objective function is different for each inversion method, though every

function generates error based on discrepancies between the apparent resistivity, phase, and impedance of the data and each corresponding block resistivity (Rodi, 2001). The total error is used to evaluate the validity of the model, and it is often represented by a root mean square value given by

$$RMS = \sqrt{\frac{1}{N}(x_1^2 + x_2^2 + \cdots)} \ , \tag{9}$$

where *x* represents the discrepancy for each block and *N* represents the total number of blocks.

Once the Jacobian is generated and the error for each block is determined for the starting model, the resistivities of specific blocks are perturbed to create a new model in an attempt to lower the error (Rodi, 2001). The error for the new model is calculated and alterations that lowered the error are kept, while ones that did not are perturbed in the opposite direction. Many competing algorithms have been developed that attempt to optimize this process so that the fewest number of iterative model solutions are required. Eventually the inversion process will lower the misfit to a point that any perturbation in either direction increases the misfit. This point might represent a local minimum, rather than a global one, which would thus lead to a suboptimal model and higher error. Optimization is needed to significantly perturb the model, through changing the resistivity step size, to renew the error minimization process once the model settles at a constant misfit value (Rodi, 2001). Altering the start resistivity and other parameters can also prevent the inversion from falling into the same minima by changing how the perturbation occurs.

1.4.2 Smoothness Constrained Inversion

The inversion type called Smoothness Constrained is a least-squares method that uses a tolerance limit on the smoothing operator to generate models. The objective function for this type is given by

$$(A^T W^T W A + \mu C^T C)\Delta m = A^T W^T \Delta f \ , \tag{10}$$

where A is the partial derivative Jacobian matrix, W is the weight function operator, C is the smoothing operator, Δm is the block parameters vector, and Δf is the discrepancy vector between the model and observed data (Kaminsky, 2012). $A^T A\Delta m = A^T \Delta f$ constitutes the least-squares portion of the function, which determines how the Jacobian, and thus the model, needs to be altered to produce a lower discrepancy based on the calculated RMS error value (Rodi, 2001). Weighting is dictated by the weight operator and determines the error contribution from each data type. Error is calculated for apparent resistivity, phase, and the complex components of impedance for both the transverse electric and magnetic modes, so specific weight schemes are needed to properly estimate the error (Kaminsky, 2012). Robust weighting is standard, and it involves maximizing the error contribution from the phase and imaginary impedance for the transverse magnetic mode because of their resistance to deviations caused by signal

altering effects such as noise and measurement errors (Kaminsky, 2012). Smoothing requires nearby resistivity blocks to have similar values to produce a gradually transitioning cross-section. Including smoothing prevents the model from forcing widespread resistivity into small areas that would cause the results to be erratic and potentially divergent or infinitely increasing (Kim, 1999). This allows the resistivity blocks to reach a stable state in their minima, though smoothing also biases the data by requiring it to have a specific form. Large smoothing removes potential features from the model, which increases the error and leads to improper conclusions concerning the resistivity landscape of the cross-section, hence the usefulness of being able to choose the amount of smoothing (Kim, 1999). The tolerance limit for the Smoothness Constrained inversion type allows for proper smoothing to be chosen to produce a valid resistivity block section that can be later analyzed for geological significance.

Section 2 – Methods

The magnetotelluric method (MT) can be used to determine cross-sectional resistivity through a series of steps. Data collection involves measuring the Earth's surface electric and magnetic fields through an array of sites in the form of a time series. The time series is Fourier transformed into the frequency domain, and used to calculate a set of site-dependent impedance tensors and induction vectors for the array of site locations (Bahr, 1988). Induction vectors are representations of the vertical to horizontal magnetic field component ratio that indicate lateral conductivity variation and point toward or away from internal current concentrations depending on the convention (Simpson, 2005). Processed data form an observed set that is matched to a calculated model through inversion to indirectly generate the resistivity cross-section of the array. Multiple inversion parameters and options are chosen to reduce error and produce a valid model. This cross-section can then be analyzed for geophysical significance and compared to other studies to justify the results. These steps of data collection, data processing, inversion, and interpretation constitute the full magnetotelluric method, which is the process used for this experiment.

2.1 Field Data Collection

2.1.1 Site Arrangement

The electric and magnetic field data was measured at 31 sites constituting a portion of the iMUSH MT 3-dimensional array. Sites generally ranged from west of Mount Rainier to north of Mount Adams, so a portion of the sites were chosen to create a 2-dimensional array that projected onto a northwest to southeast line, which is shown below in Fig. 2.1. Each site was operated for two days to measure the MT responses over a broad frequency bandwidth, thus giving resistivity information for the largest possible depth range, as expressed through Eqn. 6. Installations required two widely separated sites running simultaneously to remove the influence of cultural noise via the MT Remote Reference method (Gamble, 1978), which is discussed in section 2.2.1. Field crews had

four sets of site equipment, with one set as backup, so site schedules would usually involve pulling two sites and installing them elsewhere each day.

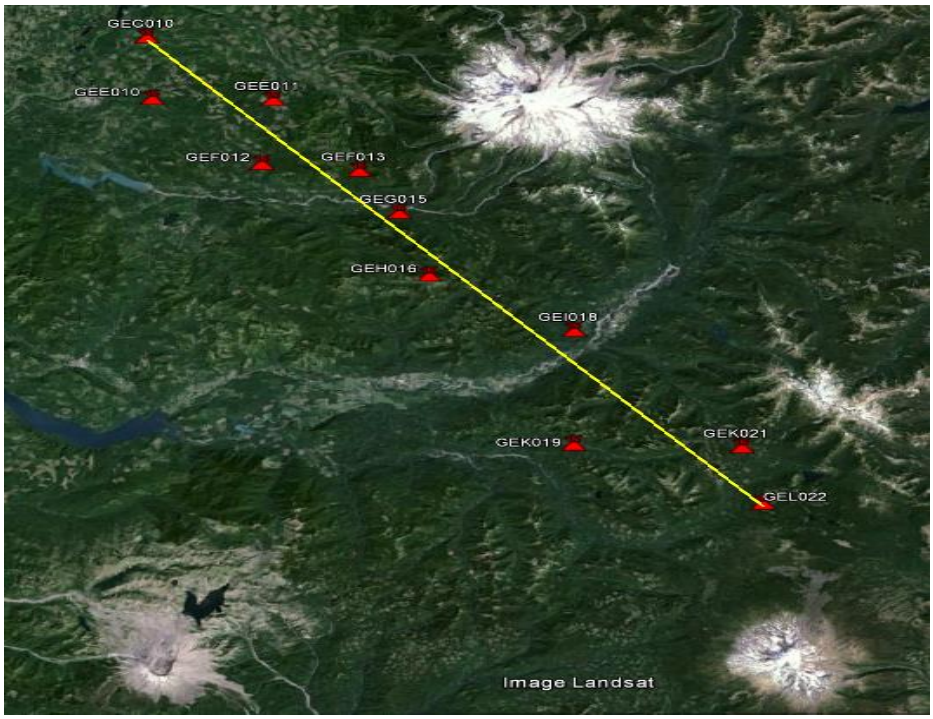

Fig. 2.1: Google Earth image of site locations and cross-section used for 2-D array, with Mount Saint Helens, Mount Rainier, and Mount Adams located on the left, top, and right respectively

The electric field was measured at each site by placing electrodes at the distal ends of 100 meter long horizontal electric dipoles oriented in the local magnetic North-South and East-West directions. Magnetic North-South corresponded to E_x and East-West corresponded to E_y represented in section 1.3.1. Since the measurement coordinate frame does not necessarily correspond to the geoelectric strike direction, it is necessary to rotate the measured impedance tensors into a frame of reference that minimizes the diagonal elements and thereby decomposes the tensor into TE and TM modes prior to 2-D inversion of the data set.

100 meter electrode spacing was selected to observe a good signal-to-noise ratio for the voltage signal difference between electrodes that is used to represent the electric field component along the given azimuth. Sites were predominantly located in wilderness areas, so cardinal direction dipoles were not always possible. This was resolved through rotation, which involved creating off-axis dipoles with larger lengths to create 100 meter cardinal dipoles after projection. Essentially, the off-axis dipole length multiplied by the cosine of the angle from the cardinal direction would have to equal 100 meters to accurately capture the electric field components. The magnetic field was measured by orienting three magnetometers in the North (x), East (y), and Up (z) directions. The z-component of the magnetic field was not needed for 2-dimensional analysis, though the results were gathered for the 3-D oriented iMUSH project. The electric and magnetic field were measured at specific intervals that related to desired frequencies and thus depths once the data were Fourier transformed.

2.1.2 Instrumentation

Pb-$PbCl_2$ was chosen for the electrode material to minimize noise due to spurious electrochemical potentials and thermal drift (Petiau, 2000). The electrodes were implanted in the ground in a cup filled with the clay mineral kaolinite, along with mud both above and below the device to ensure proper ground connection and low resistance. Wires were run from each electrode to the data acquisition device and then the resistance was checked between electrodes. Ground resistance was typically in the MΩ range, though the addition of kaolinite and mud led to electrode resistances around 1 kΩ. The voltage signal across the terminals of the electrode was typically in the millivolt range, hence the need for low resistance to prevent loss of electric field information. Zonge ANT/4 induction coil magnetometers were used to measure the magnetic field. The coils were shallowly buried in 4 foot long holes, with cables running to the data acquisition device for measurement. Changes in the magnetic field components induced currents in the respective directional coils, which were integrated by circuit boards to produce the components of the B field signal with amplitudes typically around a volt.

The Zonge Zen RX6 and the Narod Intelligent Magnetotelluric System (NIMS) were used as data acquisition devices for separate field expeditions. The Zen was powered by a 12 volt car battery and used a GPS puck to sync the time and location of the device with other systems for noise removal and run scheduling. Metadata such as site name, electrode spacing, and magnetometer ID was written to the device during scheduling. The signals could also be amplified during scheduling to maximize the signal without causing railing, which helped differentiate information from noise. The NIMS had different functionality, yet they recorded the same information in a similar manner, with the major difference being that the Zen system enabled capture of data at a higher sampling rate (up to 4 kHz) and a higher resolution (32-bit digitizer) than the NIMS (1 Hz fixed, and 24-bit respectively). These hardware differences enable the Zen to acquire data at higher frequencies than the NIMS, but at the cost of substantially higher power consumption. Voltage data were obtained after the site was run and then transferred to MicroSD cards in the form of values at each sampling time. Preliminary results from the data processing programs determined whether the site had to be run again or completed.

2.2 Data Processing

Data from the Zonge Zen devices were processed through programs provided with the systems, while data from the NIMS were processed through a collection of scripts and programs produced at OSU. These processing techniques essentially conducted the same operations on different file types and data formats, so the process will only be described for the Zonge data. Zonge's software package included MTMerge, MTFT24, and MTEdit. These programs converted the recorded voltage values into electric and magnetic field time series, Fourier transformed the time series into the frequency domain, and calculated the apparent resistivities and impedance tensors from the frequency domain, among other functionality.

2.2.1 Data Merging and Noise Removal

The program MTMerge combined the measured voltages over the time interval into continuous signals for each electric and magnetic direction, which changed the data into a time series that was able to be Fourier transformed. The electric field was determined from the gradient of the electric potential given by the electrode voltage and spacing in the metadata, while the magnetic field was determined from calibration files specific to each magnetometer that related the voltage to the B field value. Rotated electrode dipole orientation was compensated for by removing the overlapping portions of the noticeably different electric field signals to generate the *E* field in the cardinal directions. MTMerge could also be used to compare sites and reliably reduce cultural noise to preserve the data. Sites were spaced at least 10 kilometers apart to cause the devices to measure different cultural noise, though nearly identical magnetotelluric signals, so significant differences were attributed to noise (Gamble, 1978). The 60 Hertz band was also automatically removed from the signal because it is widely used by electrical devices. Rotation and noise removal cleaned up the time series data, which allowed for it to be properly Fourier transformed.

2.2.2 Fourier Transformation and Tensor Generation

The program MTFT24 Fourier transformed the time series into the frequency domain to allow for the electric and magnetic fields to be estimated by sinusoidal signals of varying frequency. Frequency corresponds to depth by the skin depth effect described in Eq. 6, so transforming the data allowed for the fields to be estimated at the measured depths. Impedance and apparent resistivity at each of these depths were calculated for each site location through MTEdit using the relationships in Eq. 5, and these depth related values constituted the observed data matched during inversion. MTEdit output the data in an .avg file specific to the program, so the files had to be converted into an .edi file type with values rearranged and calculated through a script to enable inversion.

2.3 Inversion Parameters and Technique

The final step for turning the data into analyzable results required 2-dimensional non-linear inversion through the program ZondMT2D (Kaminsky, 2012). Inversion involves creating a homogeneous half-space model and then perturbing it by small amounts to minimize the root mean square (RMS) error value between the measured impedance values and the results calculated from the resistance blocks of the model using Eqns. 7 and 8. Inversion has the tendency to fall into local minima where changes increase error, which is why a range of parameters were used and several program runs of many iterations were conducted to obtain valid results.

2.3.1 Model Creation and Inversion Preparation

The inversion program ZondMT2D, which was created by Alexander Kaminsky, was used to generate resistivity block models that approximated the measured electromagnetic data and constituted the results section of this research. The program is able to read observed impedance, apparent resistivity, and phase data that are output from the Zonge software package, that was previously mentioned, or other magnetotellurics based computer scripts. A starting model can be generated from options in the program, and then altered through inversion to better match the observed data. The general principles and process of inversion, including the smoothness constrained inversion type that was used, can be found in Section 1.4, while section 2.3 is concerned with the specific options and parameters of the program that were used to obtain the resistivity block models in the results.

11 sites were inverted out of the set of iMUSH project data that were collected during 2014, to generate a linear array of stations suitable for 2D inversion, while still maintaining a reasonable site spacing to cover the whole area of investigation. A mesh was constructed to set the block locations where each resistivity would correspond to a specific apparent resistivity and impedance relating to the observed depth and site location information. The default starting height/thickness and number of layers were set to 1.3 meters and 40 layers respectively. The Incremental Factor, i.e. the amount that each subsequent model layer's thickness is multiplied by relative to the thickness of the layer above it, was chosen to be 1.25 to cause the maximal depth of the model to be 391.15 kilometers. This chosen model depth exceeds the ~350 km maximum depth of sensitivity of the NIMS acquisition system used for data collection of the 11 sites. The maximum model depth was chosen to be larger than the maximum depth sensitivity of the data to prevent the model from generating unnecessary structure that cannot be justified on the basis of the measured data. Extended model width past the sites on the edges of the cross-section was also chosen for this same reason. The mesh was chosen to be regular, which means that it scaled the block width to match the site spacing, though the sites were relatively evenly spaced so it did not have much of an effect. Reasonable start resistivity of the model blocks ranged from 20 to 100 Ωm according to the results from previous Cascade MT cross-sections, and one of the main methods of verifying the results was through varying this parameter (Stanley, 1992), (Hill, 2009), (McGary, 2014). 100 Ωm start resistivity yielded the best results, with the starting model shown below in Fig. 2.2

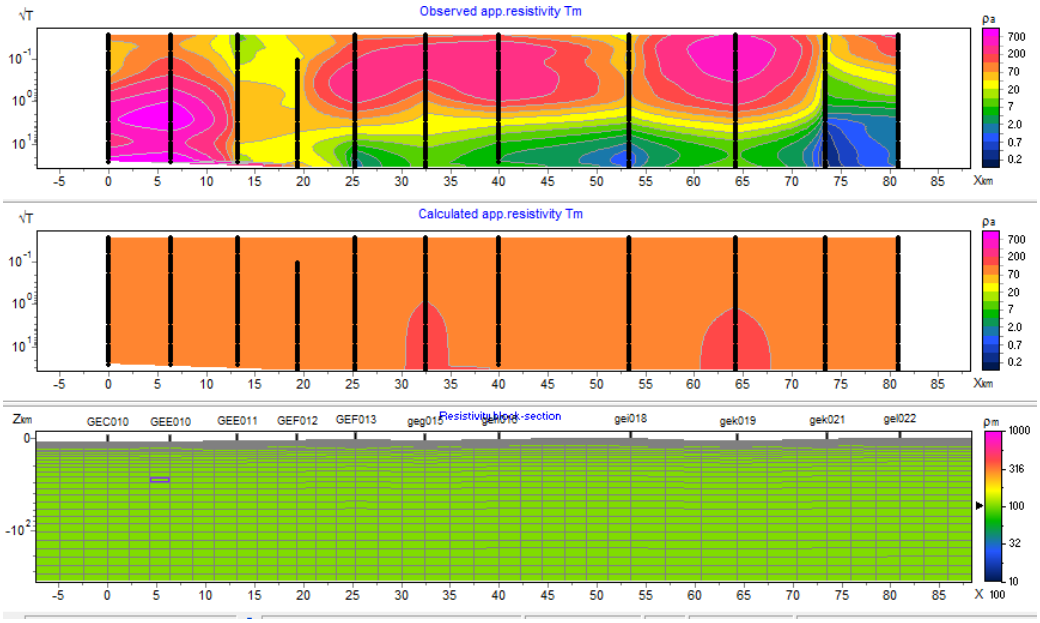

Fig. 2.2: Picture of inversion starting model of resistivity vs. depth (Z axis) in log(km) and location along northwest (left) to southeast (right) cross-section in kilometers. The bottom panel is a uniform halfspace of 100 Ωm resistivity, bounded on top by a surface that matches the topography along the surface profile. The middle panel displays the calculated transverse magnetic (TM) mode apparent resistivity generated from the starting model, and the top panel shows the apparent resistivity determined from the data along the cross-section profile. Deviations from constant apparent resistivity are attributed to topographic effects, where low points have increased values.

Fig. 2.2 depicts the transverse magnetic mode, where the magnetic field is transverse to the geoelectric strike direction, for both the observed and calculated apparent resistivities. The ZondMT2D program also determines the observed and calculated apparent resistivities for the transverse electric mode, with the electric field being transverse to the geoelectric strike direction, as well as both transverse modes for the phase and impedance of the observed data and model. The apparent resisitivity, phase, and impedence values are all matched during the iterative inversion process by altering the resistivity block model, which causes the top and middle panels of Fig. 2.2 to look increasingly similar. One transverse mode and one value type (resistivity, phase, or impedance) are chosen to be weighted greater during inversion and thus better matched, though all forms of the calculated and observed data have strong agreement in proper models.

The observed impedance was rotated to minimize Z_{xx} and Z_{yy} of the impedance tensor, which correspond to 3D effects relating to induced non-perpendicular E and B components described in section 1.3.1. 2D induction only produces perpendicular components, so minimizing the other tensor values maximized the detection of 2D structure. Galvanic distortion effects relating to fine-scale near-surface structures were also present, which were caused by abnormally high or low resistivity that significantly altered the surface measurements of all parts of the induced electric field signals by respectively forcing them away from or into the material as they diffused (Bibby, 2005). The magnetic field is relatively immune to galvanic distortion because it is composed of

the integrated inductive effects of the electric field at all depths, so the distorted near-surface field components only have a small effect. The effects of galvanic distortion were reduced through adding a surface layer and the static shift i.e. galvanic distortion removal option. Adding a surface layer allowed the program to place resistivity above the model where it could not affect the resistivity calculations, so the extreme resistivity structures were moved there to lessen the effect on lower blocks. Static shift removal involved algorithmic detection and negation of the effects on the impedance data through a process known as tensor stripping (Bibby, 2005).

2.3.2 Inversion and Optimization

Inversion of the impedance data began after the model was created and adverse effects on the data, such as 3D structures and static shift, were minimized. Impedance was chosen to be inverted because it yielded lower error and better results than inverting the apparent resistivity and linear or log phase. The real and imaginary portions of the impedance were inverted for the transverse electric and magnetic modes with a robust weighting scheme. The default Smoothness Constrained inversion type was chosen, because the program was optimized for it and large smoothing increases error. Model topography determines the depth that data measurements correspond to based on the elevation of the cross-section, and absolute coordinates of the sites were used rather than an elevation model, due to the relatively low height change along the cross-section. The inversion was started once all of these options and parameters were chosen.

Optimization began once the objective function representing the resistivity block values of the model fell into a local minimum and reached an RMS misfit plateau for many iterations. The objective function perturbs the resistivity blocks to reduce misfit, which ceases when the error component reaches a minimum, so different iteration methods than normal inversion were needed to change the tested block values beyond the region where the model became trapped. First, the robust weighting scheme was removed to increase the importance of the real impedance component to change how the RMS was determined and to thus find a new local minimum. Inversion continued with this new weighting until the model hit a new and lower RMS plateau. The robust weighting scheme was then applied again and the full optimization option was selected, which changes the perturbation steps of the model when reducing error. This allowed the model to calculate new potential resistivity solutions to the observed impedance that reduced misfit further. Full optimization was used until the inversion hit yet another RMS plateau, where the optimization was changed to Length step with a perturbation change designed to lower the misfit further (Kaminsky, 2012). Length step inversion was continued until the RMS misfit reached a plateau, which constituted the lowest possible value for the generated block section. This resistivity block section model is the primary result of the experiment, because it is the most accurate representation of the conductivity landscape for the surveyed area that could be produced.

Section 3 – Results

The resistivity block section seen below in Fig. 3.1 constitutes the best fitting model that was produced from the data collected for the cross-section. A large combination of parameters and options were tested to produce the lowest RMS error model that was geophysically reasonable for the cross-section. The number of surface layers, inclusion of static shift removal, starting model resistivity, and inversion algorithm type were all varied extensively and compared to come to the conclusion of minimal model error. A misfit of 1.44 RMS was reached from including one surface layer, using static shift removal, having a start resistivity of 100 Ωm, and inverting the impedance data. All of the other options led to higher RMS misfit values except when the same parameters were used without static shift removal, though an explanation of the unreasonableness of the model will be given shortly. It is highly unlikely to be able to produce a model with an RMS error that achieves the statistically expected target value of 1 RMS, since the statistical assumptions that go into estimating the variance of each impedance estimate are satisfied only approximately. Other factors, such as deviations from the plane wave assumption for the signal source from cultural electromagnetic noise sources, can impact the size of the impedance tensor element's error bars to further affect the model error. As a consequence of these factors, models that attain a value of less than 2 are generally accepted, particularly if the resulting models are consistent with models derived from other geophysical and geological studies. A misfit of 1.44 RMS is well below the guideline of 2, and thus the model can be accepted as valid and representative of the resistivity landscape of the area if it can be checked with preexisting studies. This check will occur in the discussion section, though it is also important to analyze the agreement between the model and data to confirm that the program reported the RMS correctly.

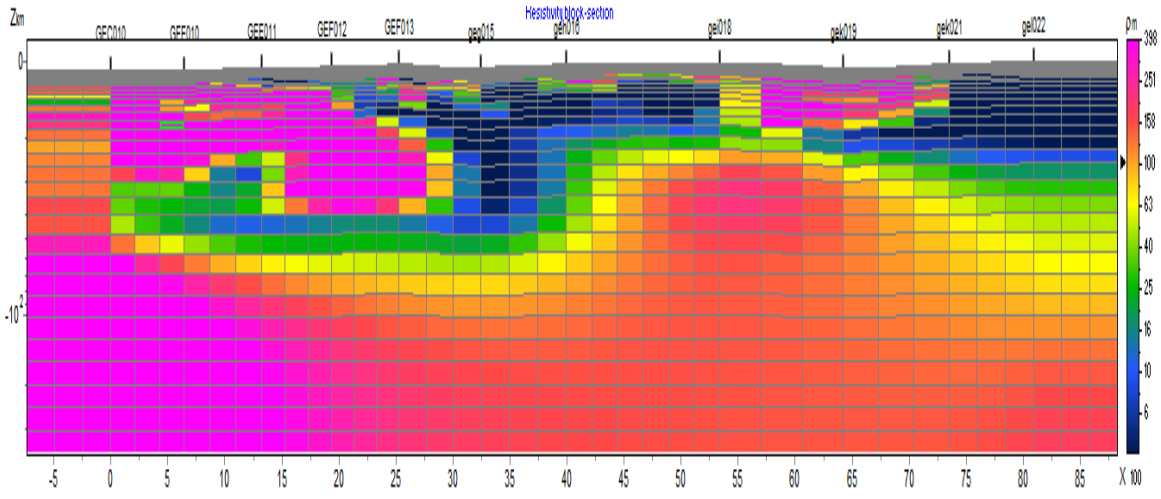

Fig. 3.1: 1.44 RMS final resistivity block section with static shift removed for model depth in log(km) (*z* axis) vs. position along northwest to southeast cross-section in kilometers (*x* axis). The color code on the right indicates that blue is conductive and red/purple is resistive.

Assessment of the 1.44 RMS error value can be done through examining the pseudosections of the observed data and model results for each of the data types in Fig. 3.2 below, as well as Figs. A.1 and A.2 in the appendix. Pseudosections show the effective values vs. period (1/frequency, which is a proxy for depth through the skin depth relationship) and location along the cross-section to give a general form of the data type, so they are useful for visually determining the agreement between the model and measured data. There is a near-perfect match for the impedance values, because it was the data type chosen to be matched for inversion, yet the other figures also show strong agreement between the calculated and observed data. This agreement between the model and observed data types leads to the conclusion that the reported error is most likely correct or at the very least within the accepted range.

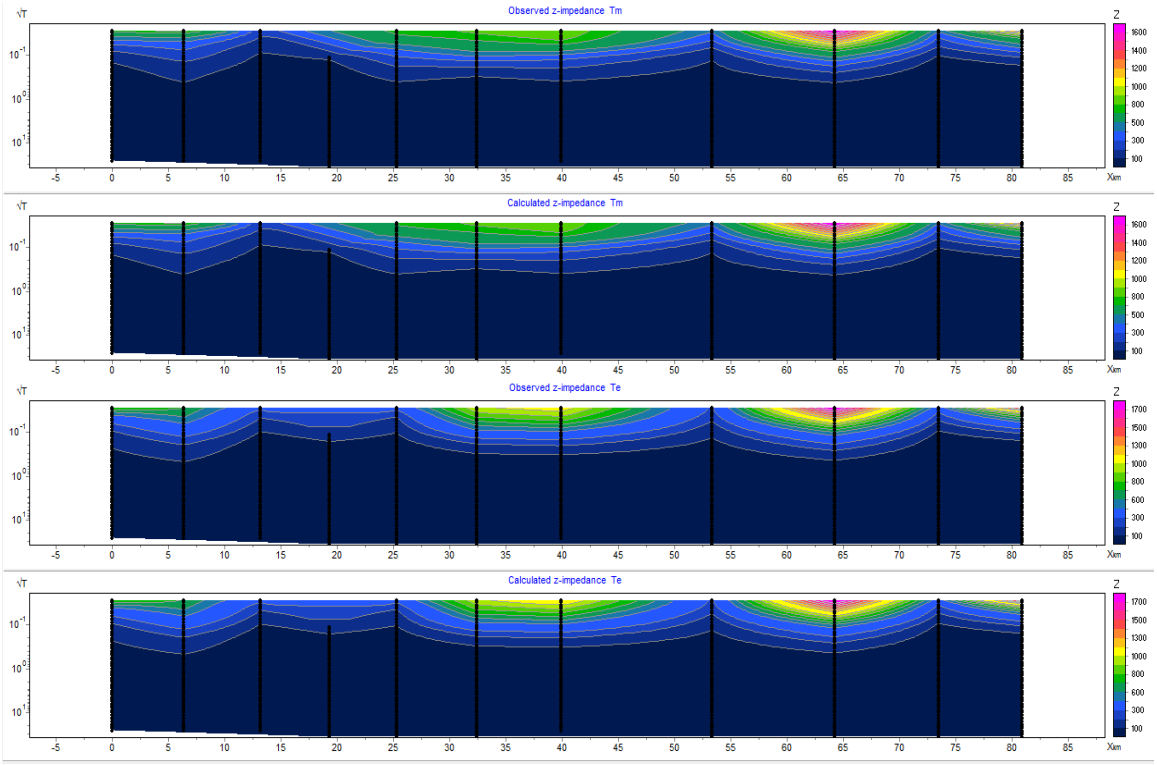

Fig. 3.2: Pseudosections of effective model depth (*z* axis) vs. cross-sectional location in kilometers (*x* axis) for the observed and model impedances of the transverse magnetic and electric modes shown on the top and bottom respectively. Red/purple corresponds to high impedance, while blue corresponds to low impedance.

The 1.32 RMS resistivity block section displayed below in Fig. 3.3 serves as the only model produced that had a lower error than the accepted 1.44 RMS results. This model is unrealistic despite the low error because of its resistivity landscape. Extremely low resistivity from the SWCC has only ever been found to extend to a maximum depth of approximately 25 kilometers, yet the block section shows similar values beyond 40 kilometers in certain areas. These resistivities do not line up with any existing cross-sections, nor do they make geophysical sense considering that marine sediment would have metamorphosed well above that depth and melt has a specific upwelling pattern that

the section does not reflect. This discrepancy leads to the conclusion that the 1.32 RMS model does not accurately represent the site profile, which shows the importance of including static shift removal to counteract galvanic distortion caused by the high presence of shallow conductivity in the area. Rejecting the 1.32 RMS model enables the conclusion that the 1.44 RMS model is the best potential result from the collected data, given that it has the lowest RMS value and a proper geophysical form.

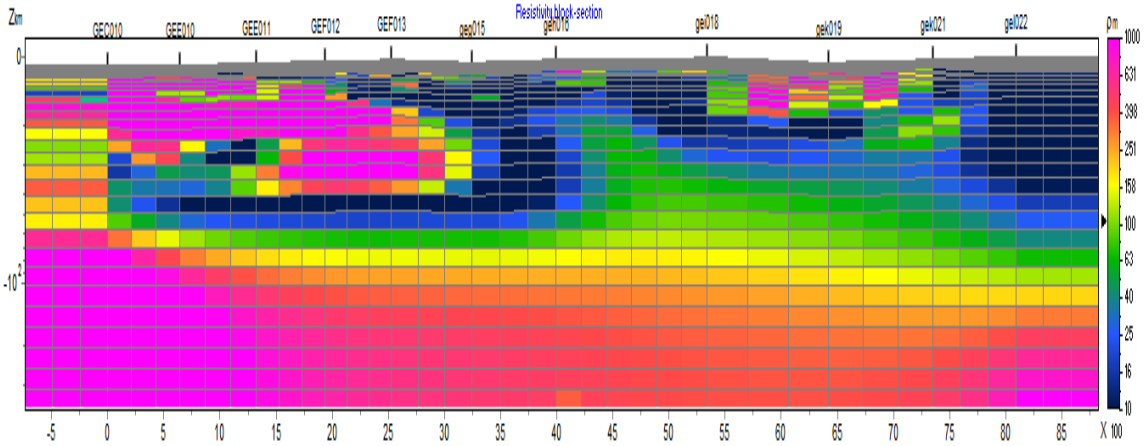

Fig. 3.3: 1.32 RMS resistivity block section without static shift removal for model depth in log(km) (*z* axis) vs. cross-sectional position in kilometers (*x* axis). Red/purple corresponds to low conductivity and blue relates to high conductivity.

The only step left for validating the results and drawing conclusions is to compare the best potential model with preexisting geophysical surveys to confirm the form of the resistivity. MT generated resistivity block sections are the primary source of previous models for the areas near the cross-section, though a seismic study was also done along the Skate Mountain anticline corresponding to a portion of the line. Both imaging types were focused on the upper 40 kilometers of the Earth where volcanism and the SWCC are present, so the related portion of the 1.44 RMS block section is shown below in Fig. 3.4 for comparison in the discussion section.

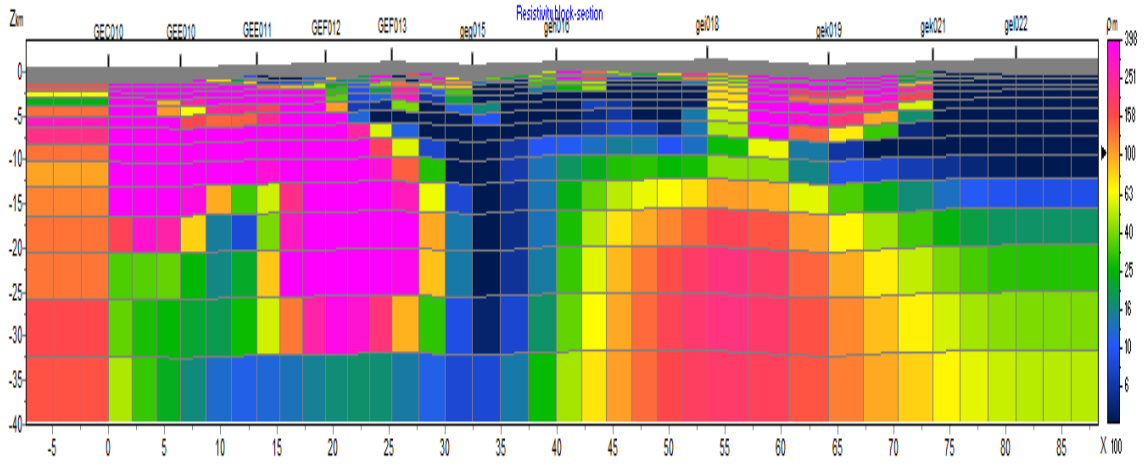

Fig. 3.4: 1.44 RMS resistivity block section with static shift removed for low linear model depth in kilometers (*z* axis) vs. cross-sectional position in kilometers (*x* axis).

Section 4 – Discussion

There are three main surveys consisting of the work of McGary *et al*. (2014), Stanley *et al*. (1992), and Hill *et al*. (2009) that can be analyzed to validate the results because of cross-sectional overlap between their studies and this experiment. The gently dipping high resistivity shown in Fig. 1.3 that corresponds to the subducting Juan de Fuca/Gorda plate overlaps with the highly resistive body starting at a depth of around 50 kilometers on the northwest (left) portion of the results in Fig. 3.1, so that segment of the block section can be attributed to the plate (McGary, 2014). This correlation between models does not have an effect on the interpretation of the results, because the geophysically important information resides at shallow depth, though it does help to confirm the results.

There are two sections of overlap for the trapped marine sediment survey, with one being an MT generated resistivity comparison in Fig. 4.1 and the other a seismic study in Fig. 4.2. The MT survey overlap corresponds to the region from sites C010 through E011 in Fig. 3.4, which has a high presence of non-marine resistive sediment according to the section west of Mount Rainier on the lithology map in Fig. 1.5. The resistivity models in Fig. 4.1 show the same general form and values, with a low resistivity section of 5 to 30 Ωm starting around 20 km deep and rising up to 15 km depth as the cross-section goes eastward. A highly resistivity portion sits on top of the low resistivity shape in both cases, and the 250 Ωm model value fits within the 100-250 Ωm range of the left figure. Resistivity is not above 100 Ωm below 25 km depth on the 1.44 RMS model, though that value was chosen in the Stanley *et al*. (1992) figure to represent unresolvable results due to computational limitations at the time. The models do not have identical shape, due to the use of different display techniques, yet the overall agreement of values and trends supports the 1.44 RMS model.

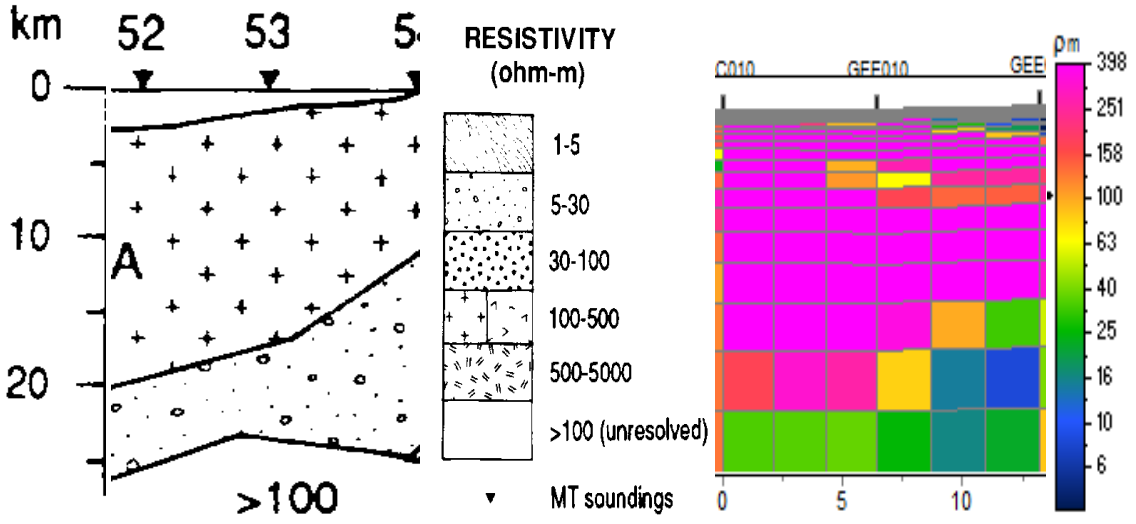

Fig. 4.1: Comparison of equivalent depth resistivity for overlapping cross-sections of the Stanley et al. (1992) survey and the 1.44 RMS model. Both cross-sections correspond to a region west of Mount Rainier.

Fig. 4.2 was generated by a deep seismic reflection study along the Skate Mountain anticline, which is shown in Fig. 1.3. The survey was conducted by placing seismic vibrators along the anticline and then measuring reflections that occurred (Stanley, 1992). Density and compositional boundary locations were determined from the separation of time between creating the seismic waves and receiving them after reflection from a boundary. The boundary lines are shown in Fig. 4.2 as black lines, and the middle layer was determined to be an Eocene marine unit from the geological structure and reflection values (Stanley, 1992). Seismic depth for the figure corresponds to 0 to 8 kilometers, so the marine layer's shape can be compared to the upper portion of Fig. 3.4.

Fig. 4.2 shows an eastward plunging layer of the Skate Mountain anticline corresponding to the SWCC that starts flat and has a hump right where it starts to increase in depth. This exact form is shown in the low resistivity portion of the 1.44 RMS block section where the cross-section runs along or nearby the anticline. The low resistivity portion starts flat between sites F12 and F13 at 5 km depth in Fig. 3.4 and starts the plunge/hump portion between sites F13 and G15. Low resistivity continues to deepen until it reaches site H016, where the cross-section diverges from the anticline. The strong agreement between the conductivity shapes of both surveys helps to strengthen the argument for the validity of the 1.44 RMS model.

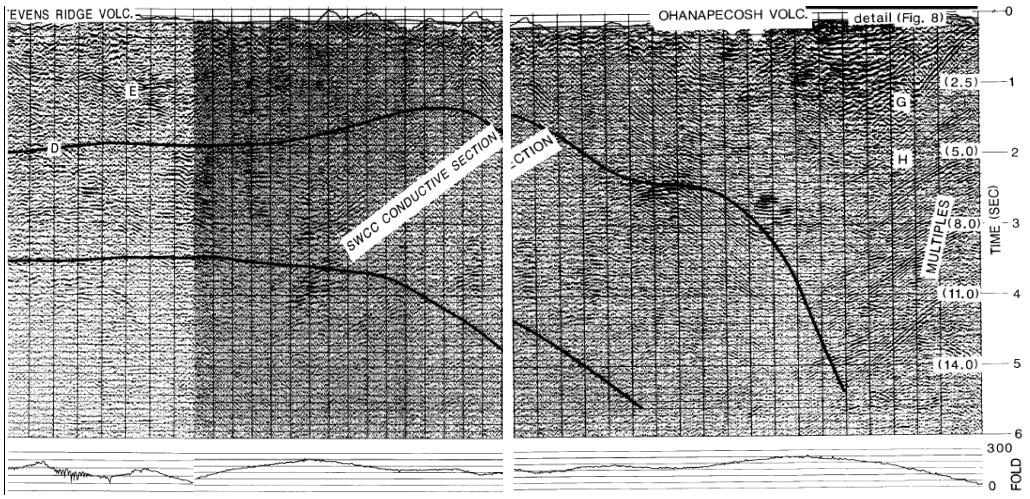

Fig. 4.2: Seismic depiction of the SWCC conductive section along the Skate Mtn anticline (Stanley, 1992).

The overlap section for the Hill *et al*. (2009) MT survey corresponds to a small portion of Mount Adams ranging from 2 kilometers west of its peak to 5 km east of the peak. This span represents approximately 20 km of the 1.44 RMS model because it runs northwest to southeast, and the northward component adds extra distance when comparing with the east-west Hill *et al*. (2009) results. Both resistivity models have a shallow high resistivity chunk on the westernmost portion of the section and a general eastward rising conductivity around 10 km deep. There is a slight disagreement between

the maximum depth of the very low resistivity material, and the shape of the deeper high resistivity has opposite dipping direction. The 1.44 RMS model also has generally lower near-surface conductivity, despite having a cross-section a few kilometers north of Mount Adams and the Hill *et al*. (2009) cross-section. The portion of the cross-section for the 1.44 RMS model shown in Fig. 4.3 corresponds to an area of previous lava flows and frequent volcanic activity depicted in Fig. 1.4, so it seems reasonable to attribute the minor difference between the models to their seperation rather than fundamental geophysical differences. Comparing the two models does not add much support to the validity of the 1.44 RMS results, yet it does give a potential interpretation for the easternmost part of the resistivity block section as having a volcanic basis.

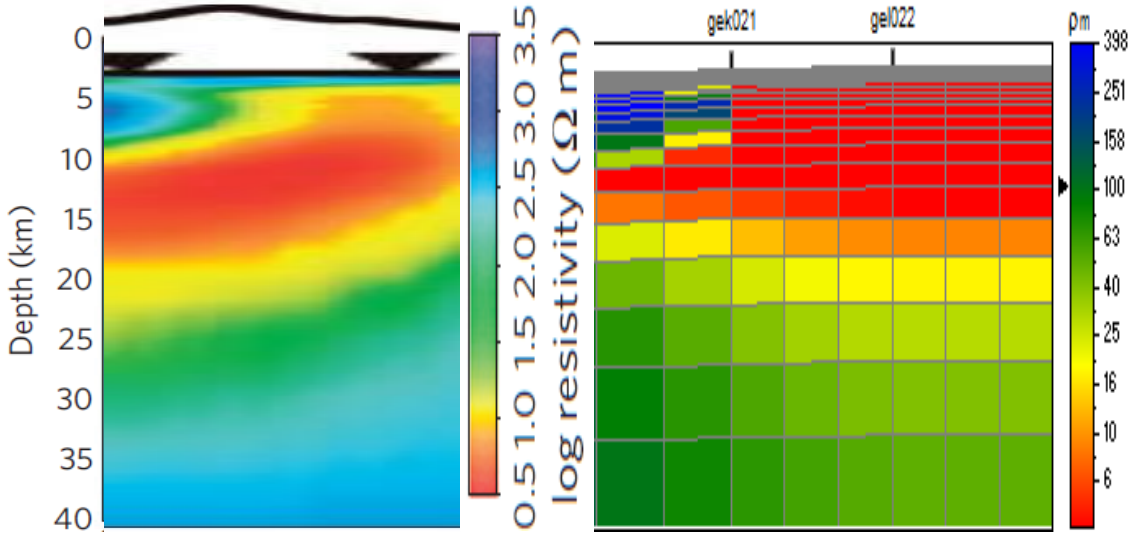

Fig. 4.3: Comparison for equal depth resistivity for overlapping cross-sections of the Mount Adams portion of the Hill et al. (2009) survey and the resistivity color inverted 1.44 RMS model.

Sites I18 and K19 were not represented in any of the comparisons with preexisting surveys because their line projected positions had significant separation from all of the past cross-sections. The absence of these sites caused approximately a third of the cross-section from H16 to the western part of Fig. 4.3 to lack verification against other models. Strong agreement in form, depth, and values between the other portions of the cross-section and the comparative models can potentially make up for this gap, given that the model has acceptably low error and a reasonable geophysical form based on the presence of shallow conductivity when sites were located on the SWCC. Each of the important resistivity shapes, including the northwestern resistive blocks, the central plunging conductivity, and the southeastern shallow resistive and conductive portions, were matched to other models, so it seems reasonable to extend the validity to the entire cross-section. The ability to adequately match the best possible results from the measured data to multiple previous geophysical surveys verifies that the 1.44 RMS model most likely accurately represents the resistivity landscape of the area corresponding to the cross-section. Verification of the model therefore allows for conclusions to be suggested concerning the area studied.

Section 5 – Conclusion

The purpose of this project was to obtain measurements for a cross-section that runs through the southern Washington Cascades volcanic triangle and that intersects previous surveys, so that interpretations concerning the geophysical properties of the area could be drawn. Data were collected and modeled through inversion to produce a resistivity landscape that had a low enough error, as well as verification from general agreement with previous models, to be declared a reasonable representation of the ground along the cross-section. This representation, shown in Figs. 3.1 and 3.4, can now be analyzed for geophysical significance based on the shapes of the resistivity blocks and their locations with respect to the geology of the region.

The Southern Washington Cascades Conductor (SWCC) and arc volcanism are the dominant geophysical factors in the area that was studied. Every segment of shallow elevated electrical conductivity on the block section corresponded to a location where the marine sediment based SWCC is located, except for one. The only other shallow conductivity present in the block section corresponded to upwelled magma from the nearby volcanism of Mount Adams, which was matched to the MT cross-section of Hill *et al* (2009). Each area of high resistivity corresponded to an area not in the marine sediment based SWCC or in close proximity to a volcano, and the resistivities were also confirmed with the results of Stanley *et al.* (1992) and Hill *et al.*(2009). This strong agreement between conductivity and the presence of marine sediment or volcanism seems to suggest that the cause of conductivity can be determined by geographical location with regard to ground composition and volcano proximity. Thus, areas of shallow conductivity within the volcanic tringle could potentially be attributed to trapped marine sediment, and elevated crustal conductivity near the volcanoes could be declared to be partial melt or magma.

The problem with concluding that geography dictates the conductivity cause is that there is a region on the cross-section where trapped marine sediment is actively being brought to the surface near Mount Rainier. The plunging conductivity relating to the Skate Mountain anticline can be seen in Fig. 3.4 from in between sites F12 and F13 to just before site H16, yet there is also what appears to be a mid-crustal conductor similar to the one shown in Fig. 1.5 that could correspond to an upwelling partial melt that would cause a rising conductivity resembling a plunging marine layer. Both causes have similar forms and conductivities, so it is very difficult to distinguish them and ascertain the true reason for the conductivity shape. The potential mid-crustal conductor has the same value as the one shown in Fig. 1.5, yet it starts almost twice as deep. Another issue is that the cross-section runs tangential to Mount Rainier, rather than directly at it like in the preexisting survey, so it seems strange that magma would form and upwell near the surface in a location away from the volcano. It is impossible to deny the presence of trapped marine sediment in the area, given that the anticline is actively bringing it to the surface through erosion, yet that explanation cannot address the deep conductivity. The inability to decide between the two causes is important because it establishes a need for further investigation before concluding the nature of the entire Cascade triangle.

Overall, it seems reasonable to attribute conductivity to trapped marine sediment or volcanism in areas where the other factor is not present, yet that conclusion cannot be adequately supported without joint interpretation with other survey types in the same region. The shallow conductivity from site H16 to I18 in Fig. 3.4 certainly seems to be related to trapped marine sediment, and there are no other explanations for the conductivity from K21 eastward beside volcanism, though no definitive declaration can be made concerning their natures. It also seems more probable that a plunging layer of marine sediment is the cause for the central conductivity shape, rather than an upwelling mid-crustal conductor, but that is only an argument based on likelihood and reasonability. It is important not to overanalyze a limited data set in a geophysically complex area, so potential causes and explanations are all that can be presented here without reaching potentially incorrect conclusions. Ultimately, a full survey of varied imaging techniques is needed to study the entire region and reach a final conclusion concerning the nature of the Cascade triangle. This full survey is called the iMUSH project, which this experiment was a part of, and it constitutes the future work of this investigation. The 2D MT survey was useful for focusing the overarching study and providing potential causes of conductivity in the area, despite being unable to reach any definitive conclusions concerning the geophysical properties of the triangle containing Mount Saint Helens, Mount Rainier, and Mount Adams.

Acknowledgements

This thesis analyzed data collected for the imaging Magma Under Saint Helens (iMUSH) project, so it was indirectly financially supported by the GeoPRISMS and Earthscope programs of the US National Science Foundation (NSF). A license for the inversion program ZondMT2D that was used to generate the results of the thesis was generously donated by Alexander Kaminsky, the creator of the program, so I would like to thank him. I would also like to thank my mentor Adam Schultz for allowing me to work on this project and for overseeing the whole process. Graduate students Esteban Bowles-Martinez and Brady Fry assisted in inversion and data processing respectively. Esteban taught me the art of script writing and also gave helpful tips and starting parameters for inversion, while Brady instructed me on data processing methods and helped to rotate and remove noise for the data that were collected. Kyle McDonald coordinated data collection and led one of the field crews that I was on. Paul Bedrosian and his United States Geological Survey (USGS) crews collected a significant portion of the data, including Jared Peacock's group who measured all of the sites that were analyzed for the results of this thesis. My work on the project included data collection for sites that were not part of the 2D cross-section, though they were useful for the iMUSH project, data processing for many of the sites that I collected, writing a script that converted the processed data into a form useable for inversion, conducting countless inversions of varying parameters to produce proper results, analysis of the results with regard to ground composition and the SWCC, and writing this thesis. I would also like to thank my friends and family for encouraging my love of science and for supporting me throughout the research process.

References

Bahr K., Interpretation of the magnetotelluric impedance tensor: regional induction and local telluric distortion, *J Geophys* **62**, 119 – 127 (1988).

Bibby H., Caldwell T., & Brown C., Determinable and non-determinable parameters of galvanic distortion in magnetotellurics, *Geophys. J. Int.* **163**, 915 – 930 (2005).

Defant M. & Drummond M., Mount St. Helens: Potential example of the partial melting of the subducted lithosphere in a volcanic arc, *Geology* **21**, 547 - 550 (1993).

Gamble T., Goubau W., & Clarke J., Magnetotellurics with a remote magnetic reference, *Geophysics* **44**, 53 – 68 (1979).

Garcia X. & Jones A., Atmospheric sources for audio-magnetotelluric (AMT) sounding, *Geophysics* **67**, 448 – 458 (2002).

Griffiths D., *Introduction to Electrodynamics* Vol. 4, 364-395 (2012).

Hill G., Caldwell T., Heise W., Chertkoff D., Bibby H., Burgess M., Cull J., & Cas R., Distribution of melt beneath Mount Saint Helens and Mount Rainier inferred from magnetotelluric data, *Nature Geoscience* **2**, 785-789 (2009).

Kaminsky A., ZONDMT2D User Manual, 1-45 (2001-2012).

Kelbert A., Schultz A., & Egbert G., Global electromagnetic induction constraints on transition-zone water content variations, *Nature* **460**, 1003-1006 (2009).

Kim H., Song Y., & Lee K., Inequality constraint in least-squares inversion of geophysical data, *Earth Planets Space* **51**, 225-259 (1999).

McGary S., Evans R., Wannamaker P., Elsenbeck J., & Rondenay S., Pathway from subducting slab to surface for melt and fluids beneath Mount Rainer, *Nature* **511**, 338-340 (2014).

Ni H., Keppler H., & Behrens H., Electrical conductivity of hydrous basaltic melts: implications for partial melting in the upper mantle, *Contrib. Mineral Petrol* **162**, 637 – 650 (2011).

Parker R., Understanding Inverse Theory, *Ann. Rev. Earth Planet. Sci*.**5**, 35 – 64 (1977).

Parker R., The Magnetotelluric Inverse Problem, *Geophysical Surveys* **6**, 5 – 25 (1983).

Petiau G., Second Generation of Lead-lead Chloride Electrodes for Geophysical Applications, *Pure and Applied Geophysics* **157**, 357 – 382 (2000).

Revil A. & Glover P., Nature of surface electrical conductivity in natural sands, sandstones, and clays, *Geophysical Research Letters* **25**, 691 – 694 (1998).

Rodi W., Nonlinear Conjugate Gradients Algorithm for 2-D Magnetotelluric Inversion, *Geophysics* **66**, 174-187 (2001).

Simpson F. & Bahr K., *Practical Magnetotellurics*, 15-36 (2005).

Stanley W., Tectonic Study of Cascade Range and Columbia Plateau in Washington State Based Upon Magnetotelluric Soundings, *Journal of Geophysical Research* **89**, 4447 – 4460 (1984).

Stanley W., Deep Crustal Structure of the Cascade Range and Surrounding Regions From Seismic Refraction and Magnetotelluric Data, *Journal of Geophysical Research* **95**, 19419 – 19,438 (1990).

Stanley W., Finn C., & Plesha J., Tectonics and Conductivity Structures in the Southern Washington Cascades, *Journal of Geophysical Research* **92**, 10179 – 10193 (1987).

Stanley W., Gwilliam W., Latham G., & Westhusing K., The Southern Washington Cascades Conductor – A Previously Unrecognized Thick Sedimentary Sequence?, *AAPG* **76**, 1569-1585 (1992).

Tarbuck E., Lutgens F., & Tasa D., *Earth: An Introduction to Physical Geology* Ed. 11, 56-57 (2013).

Telford W., Geldart L., & Sheriff R., *Applied Geophysics*, 302-310 (1990).

Appendix

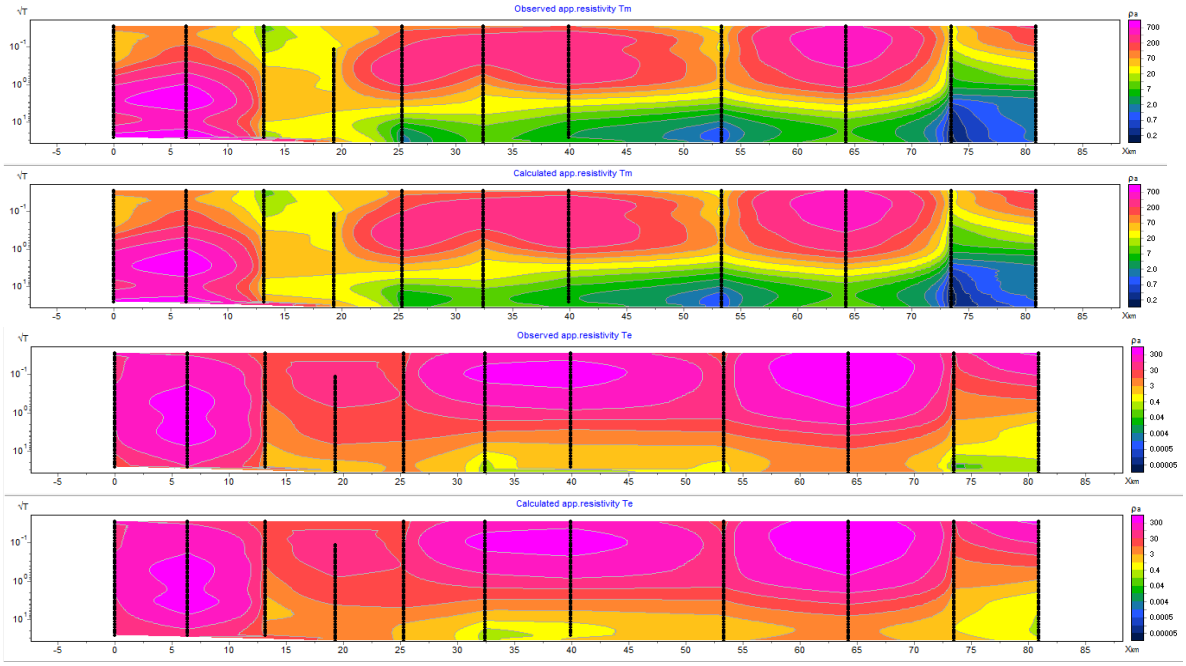

Fig. A1: Pseudosections of the observed and model apparent resistivity for the transverse magnetic and electric modes shown on the top and bottom respectively.

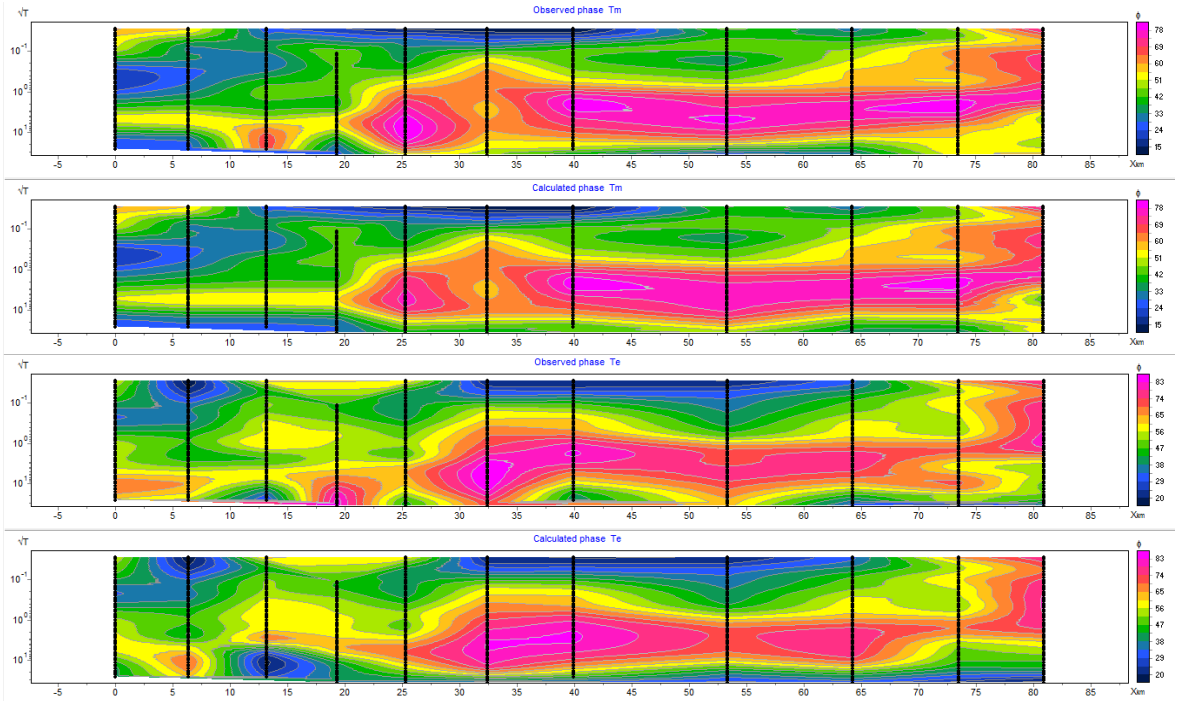

Fig. A2: Pseudosections of the observed and model phase for the transverse magnetic and electric modes shown on the top and bottom respectively.